Published in final edited form as:
Biochemistry. 2004 June 22; 43(24): 7653–7662.

Exploring Molecular and Mechanical Gradients in Structural Bioscaffolds†

J. Herbert Waite[*,‡], **Helga C. Lichtenegger**[§], **Galen D. Stucky**[⊥], and **Paul Hansma**[‖]
Department of Molecular Cell and Developmental Biology, Department of Chemistry and Biochemistry, and Department of Physics, University of California, Santa Barbara, California 93106, and Institute for Materials Science and Testing E308, Vienna University of Technology, Favoritenstrasse 9-11, A-1040 Wien, Austria

Abstract

Most organisms consist of a functionally adaptive assemblage of hard and soft tissues. Despite the obvious advantages of reinforcing soft protoplasm with a hard scaffold, such composites can lead to tremendous mechanical stresses where the two meet. Although little is known about how nature relieves these stresses, it is generally agreed that fundamental insights about molecular adaptation at hard/soft interfaces could profoundly influence how we think about biomaterials. Based on two noncellular tissues, mussel byssus and polychaete jaws, recent studies suggest that one natural strategy to minimize interfacial stresses between adjoining stiff and soft tissue appears to be the creation of a “fuzzy” boundary, which avoids abrupt changes in mechanical properties. Instead there is a gradual mechanical change that accompanies the transcendence from stiff to soft and vice versa. In byssal threads, the biochemical medium for achieving such a gradual mechanical change involves the elegant use of collagen-based self-assembling block copolymers. There are three distinct diblock copolymer types in which one block is always collagenous, whereas the other can be either elastin-like (soft), amorphous polyglycine (intermediate), or silk-like (stiff). Gradients of these are made by an incrementally titrated expression of the three proteins in secretory cells the titration phenotype of which is linked to their location. Thus, reflecting exactly the composition of each thread, the distal cells secrete primarily the silk– and polyglycine–collagen diblocks, whereas the proximal cells secrete the elastin– and polyglycine–collagen diblocks. Those cells in between exhibit gradations of collagens with silk or elastin blocks. Spontaneous self-assembly appears to be by pH triggered metal binding by histidine (HIS)-rich sequences at both the amino and carboxy termini of the diblocks. In the polychaete jaws, HIS-rich sequences are expanded into a major block domain. Histidine predominates at over 20 mol % near the distal tip and diminishes to about 5 mol % near the proximal base. The abundance of histidine is directly correlated to transition metal content (Zn or Cu) as well as hardness determined by nanoindentation. EXAFS analyses of the jaws indicate that transition metals such as Zn are directly bound to histidine ligands and may serve as cross-linkers.

Many of the earliest life forms, amoebae, slime molds, and jellyfish among others, have the consistency of pudding or tofu. The evolution of stiffer scaffolds for frame, integument, and appendages signaled better support and distribution for the mass of living tissue and contributed

†Funding for this research was provided in part by the NASA-University Research Engineering and Technology Institute on Bioinspired Materials (BiMAT) under Award NCC-1-02037, the NIH-Bioengineering Research Partnership programs (Grants DE014672 and DE015415), and NSF Grant CHE-0132443. H.C.L. thanks the Fonds zur Förderung der Wissenschaftlichen Forschung (FWF, Austrian Science Funds) for support under Grant Nos. J2028 and J2184.

* Corresponding author. E-mail: waite@lifesci.ucsb.edu. Fax: (805) 893-7998..
‡Department of Molecular Cell and Developmental Biology, UCSB.
§Vienna University of Technology.
⊥Department of Chemistry and Biochemistry, UCSB.
‖Department of Physics, UCSB.

to an enormous diversification of life forms at all levels of phylogeny. Sponges and unicellular organisms such as foraminifera, diatoms, and radiolarians live inside intricately sculpted basket-like scaffolds. The shells, bones, spicules, tendons, and carapaces of higher organisms are familiar even to casual biologists. Despite the obvious advantages of stiffer scaffolds, it is very probable that their evolution required subtle and complex parallel adaptations. We say *probable* because the challenges associated with life in a scaffold are predicted largely from nonbiological systems. Suresh (*1*) referred to the chief mechanical difficulty arising from the apposition of a stiff scaffold with a softer hydrogel as “contact deformation and damage”. An intuitive metaphor of this difficulty is a wicker basket filled with blackberries; the berries in contact with the wicker invariably get mauled. The fact that scaffolds are widespread in nature despite predictions of damage where scaffold meets protoplasm suggests that in nature contact deformation is effectively counteracted, and it becomes the challenge for experimental science to discover how this is achieved.

Our aim here is to define the physical basis for contact deformation between two materials and then to describe how two model biomolecular structures, byssal threads and worm jaws, appear to remedy this by the ingenious use of gradients and metals.

Critical Properties: Focus on Stiffness

With the use of terminology espoused by Vogel (*2*), useful solid objects can be hierarchically divided into materials, structures, and systems. In this sense, steel is a material, a nail is a structure, and the frame of a house is a system. The properties of structures made from specified materials under defined conditions can be directly tested, but in complex systems, properties are usually predicted using engineering principles. Materials have many properties, but there are a few that are so fundamental that they are considered design-limiting in the manufacture of any complex system. Critical mechanical properties include stiffness, yield strength, fracture toughness, and fatigue ratio (= ratio of fatigue strength to tensile strength) (*3*). Stiffness is technically known as Young’s modulus or initial modulus and is represented by E_i [in units of N/m^2 = Pa]. It can be determined for any material in tension, compression, or shear from the linear portion of the stress–strain curve according to Hooke’s law, $E_i = \sigma/\varepsilon$, where σ is stress [also in units of N/m^2 = Pa] or force divided by cross-sectional area, and ε is strain or change in length divided by initial length [in units of m/m]. Conceptually, E_i can be understood in terms of springs: the higher the value, the stiffer the spring. The E_i of many biological materials, including silk, skin, bone, hair, and tendon, has been measured (*2*, *4*). The stiffness of biological materials, however, is rarely a simple matter in that purely elastic (spring-like) or purely viscous (dashpot-like) behavior probably does not occur (*5*). There have been attempts to depict biological materials as combinations of springs and dashpots, with varying degrees of success, because none of these models is a very good representation of actuality. Biological materials are not as homogeneous as many of their synthetic counterparts; in addition, they are hydrated and chemically dynamic, often undergoing continuous change or remodeling throughout the life of the organism. Measured E_i will thus be highly dependent upon sample history and test conditions such as relative humidity, strain rate, and pH, among others.

Concept of Mismatch

When two materials are brought into intimate contact, the mismatch in their respective stiffness values determines how readily contact deformation will occur. Predicting structural failure due to contact deformation is possible in simple and well-defined systems if the sample geometry and elastic properties of all materials are known. Let us consider, for example, a butt joint of structural materials A and B, bonded by a contact zone (Figure 1A). Loading the butt joint in tension leads to the same axial stress overall. If, however, A and B have different stiffness values, E_A and E_B, then the deformations (measured by the respective strain values ε_A and

ε_B) will differ. The difference in deformation matters most in the contact zone, where it will give rise to interfacial stresses that act normal to the applied stress, σ_z. These stresses are described by σ_r and σ_θ, interfacial radial and circumferential stress (*6*), respectively, and can be calculated according to eq 1.

$$\sigma_\theta = \sigma_r = [\nu_B - \nu_A E_B / E_A][\sigma_z / (1 - \nu_B)] \quad (1)$$

The prominent role of stiffness (E_A and E_B) in this relationship is readily apparent. The remaining variables ν_A and ν_B denote the Poisson ratios of materials A and B, respectively. The Poisson ratio indicates the degree of lateral deformation of a material subjected to uniaxial loading. For a cylinder in tension, for example, a value of 0.4 denotes that the diameter decreases by 40% per 100% increase in length. Clearly when the stiffnesses and Poisson ratios are the same, the σ_r will be zero. Holding both Poisson ratios at 0.4 and decreasing E_B relative to E_A result in a linear increase in σ_r attaining a maximum that is two-thirds of the nominal σ_y (Figure 1A). In contrast, holding the stiffness ratio at 1 and increasing the difference between Poisson ratios ν_A and ν_B result in an exponential increase in σ_r (Figure 1B). The magnitude of radial interfacial strain σ_r thus reflects the degree of mismatch and represents a key determinant of structural failure that often takes the form of delamination in the contact zone.

The above-mentioned case demonstrates the dependence of σ_r on stiffness mismatches in a manufactured butt joint. Are biological materials subject to the same limitations?

Options: Design vs Evolutionary Adaptation

Obviously, neither human manufacturing nor nature has the luxury of completely avoiding mismatches in the critical bulk properties of joined structures. The question then becomes how to reduce the likelihood of interfacial failure between structures A and B when mismatches do occur? In manufacturing, there are two options: (1) to increase the energy of interaction across the contact zone between A and B and (2) to avoid sharp boundaries between materials. The first option has been practiced for many years and is the basis for “priming” or surface coupling treatments of glass or metals that precede bonding with polymers (*5*). Note that this will not decrease σ_r in the system; rather it may raise the bar for the stress to failure. The second option, which has only recently taken root, is the manufacture of functional gradients (*1*). In other words, if material A can be processed so that it gradually or incrementally becomes material B (and vice versa), then σ_r can be dispersed over a much larger surface area and volume. Organisms may have evolved similar strategies for joining tissues with mismatched bulk properties. We know, for example, that proteins in the holdfasts that organisms such as mussels use to attach to rock and metal surfaces contain specially modified amino acids that form charge-transfer chelate complexes with surface oxides (*7,8*). This effectively corresponds to the first strategy. Two examples illustrating the use of gradients are presented below.

Gradients in Mussel Byssus

The byssus is a connective tissue peculiar to mussels (*9*). It is deposited outside the confines of living tissue and contains no cells for maintenance or repair. Byssus functions in providing mussels with secure attachment to rocks and pilings. As such it mediates contact between a very stiff inert material (e.g., rock) and very soft living tissue. Because mussel byssus is a bundle of several hundred threads, each measuring between 2 and 4 cm in length and 50 μm in diameter (in *Mytilus edulis* and *M. galloprovincialis*), every individual thread represents a unit of attachment with the distal end bonded to rock and proximal end inserted into living mussel tissue. Is it merely an inert tether between the soft animal tissues and the rock surface? Scanning electron microscopy and biomechanical studies have established that it is much more than a tether but represents a mechanically graded fiber that is significantly stiffer at the distal

end where it joins to the attachment plaque than at the proximal end where it joins to living tissue (Figure 2). In *M. galloprovincialis*, stiffness in tension at the distal end is 500 MPa, whereas at the proximal end it is only 50 MPa (*9*). This 10-fold reduction in the distal to proximal direction does not adequately compensate for the remaining mismatches with the rock (~25 GPa) or the byssal retractor muscles (0.2 MPa). These are addressed by additional adaptations vested in the plaque and stem structures, respectively, and will be described elsewhere.

The difference between the mechanically graded byssal thread and spider dragline or *Anaphe* cocoon silk, in which high stiffness is uniform (~10 GPa), may reflect differences in the processing of the two tissues: silk is spun from a pair of ampullate glands containing polymer liquid crystals (LC)[1] (*10*), whereas byssal threads are reaction-injection molded in the mussel foot from mixtures of polymer LCs exuded from at least a dozen different pores (*11*) and "locked". The mechanism involved in "locking" the molded LCs of the fiber into a solid-state structure is still under investigation, but there are two plausible candidates: covalent cross-linking and intermolecular metal–ligand bridges. The latter will be further discussed below.

Much recent work has focused on the fibrous proteins that make up the different portions of the thread. The simplest unit of structure is a trimer of preCOL chains (~80 kD each). PreCOL is a block copolymer that is trimeric because of the central collagen domain, which occupies roughly half of the preCOL. Accordingly, its other domains are the N- and C-terminal histidine-rich domains (HIS), the flanking domains, and an acidic motif (ACID) (Figure 3). Although they are not identical, the HIS, ACID, and collagen domains are highly homologous in the three known variants, preCOL-P, -NG, and -D in which the postscripts P, D, and NG denote proximal, distal and nongraded, respectively. The flanking domains, however, represent three different structural paradigms: elastin in preCOL-P, amorphous poly(glycine) in preCOL-NG, and silk fibroin in preCOL-D (*12*). Although the flanking domains of D are reminiscent of spider silk fibroins in their poly(alanine) runs separated by intervening glycine-rich sequences, the high alanine-to-glycine ratio (~1.2:1) and low serine are more suggestive of *Anaphe* silk (*13*), which is remarkably resistant to plasticization by water (*14*). On the basis of a rise of 3 Å per residue in the collagen domain, each preCOL is predicted to have a length of at least 200 nm. Aberrations in the canonical Gly-X-Y sequence of the collagen domain are known to lead to bends or kinks in the otherwise rodlike structure of collagen (*15*). PreCOL-P and -NG have a single glycine omission in their collagen domains, whereas preCOL-D has four aberrations: one glycine omission, one glycine → serine substitution, one Y omission, and one X-Y omission (*16*). The glycine → serine substitution and Y omission are separated by only four amino acids.

The molecular shape of assembled preCOLs has been explored by both transmission electron (TEM) and atomic force microscopy (AFM). TEM of both the liquid crystalline polymer secretory granules and byssal threads reveals a smectic packing consisting of "6 + 1" bundles; that is, seven trimers per unit with six hexagonally arranged on the outside and one on the inside (*17*). These can be modeled in three dimensions as flower or banana shapes; however, AFM images have only detected the banana variety (*18*), and AFM confirms the extensive smectic arrays of these banana or bent core bundles (Figure 4).

[1]Abbreviations: AFM, atomic force microscopy; dtmp-1, distal thread protein-1; EXAFS, extended X-ray absorption fine structure; LC, liquid crystal; ptmp-1, proximal thread protein-1; preCOL-D, collagen-containing precursor, distal portion; preCOL-NG, collagen-containing precursor, nongraded; preCOL-P, collagen-containing precursor, proximal portion; TEM, transmission electron microscopy; XANES, X-ray absorption near-edge structure.

Biochemical analyses of byssal threads have established that preCOL-D and -P are distributed in complementary gradients along the thread axis. These very difficult studies initially required exhaustive pepsin digestion of the threads because their intrinsic cross-linking rendered the preCOLs insoluble against any extraction. Conveniently, pepsin usually respects the native triple helical structure of the collagen domain thus allowing the D, P, and NG collagenous remnants to be compared from each thread segment (*19*). More recently, we have exploited the fact that full-length preCOLs can be recovered from KCl-induced threads (*20*) because cross-linking has not yet set in. PreCOL-D decreases from distal to proximal, whereas preCOL-P, which starts beyond midlength, increases from midlength to proximal. Figure 5A illustrates the gradients, which are roughly linear in *M. edulis* and *M. galloprovincialis* threads. PreCOL-NG, in contrast, is uniformly distributed.

It should be noted that preCOL-P and -D are not the only byssal proteins distributed as gradients. Ptmp-1, a protein with two von Willebrand type-A domain repeats, increases toward the proximal end of the thread (*21*). In contrast, a glycine-, tyrosine-, and asparagine-rich protein dtmp-1 is concentrated toward the distal end (Sagert and Waite, unpublished results). Preliminary evidence suggests that both of these are present at concentrations of < 10% those of the preCOLs and appear to serve as a matrix between the preCOL fibers.

It is not known exactly how the different preCOLs are put together to make the higher-order fibrous structures evident in the thread. Parry and Steinert (*22*) dissected the molecular structure of intermediate filaments by combining fiber X-ray diffraction with bifunctional cross-link analysis, but this approach has not been fruitful with byssal threads possibly because the density of nonreducible cross-links is already very high. An alternative interrogation of assembly has been attempted by comparing a pair of physical models using basic laws of springs (series and parallel arrangements as per ref 23) and stiffness estimates for each prominent domain as reported in the literature: 10 GPa for a water-resistant alanine-rich silk (*14*), 1.5 GPa for tendon collagen (*9*), 2 MPa for elastin (*9*), and 150 MPa for glycine-rich GGGX sequences (*24*). By applying the formula for springs in series (*23*), net moduli for preCOL-D, -NG, and -P were calculated to be 2600, 280, and 4 MPa, respectively, assuming volume fractions add up to one.

At this point, we can view preCOL-D, -NG, and -P as LEGO blocks having roughly similar lengths and diameters but with slightly different shapes (due to bends or kinks). The challenge is to find out how to arrange these in a way that is consistent with their distributions and with the measured modulus of the full thread. Given that the fibers formed appear to be continuous, two possible modes of assembly are shown in Figure 5. In the model A, preCOL-NG alternates with D or P to form microfibrils with an alternating repeat pattern, for example, D–NG–D–NG–P–NG–P–NG. The gradient would result from the different positions of P-onset in the packed microfibrils. Application of the law of parallel springs to this assembly reveals a high distal stiffness of 500 MPa descending to a proximal low of 8 MPa, or a 60-fold decrease. In model B, fibers formed from NG and D or P remain segregated, for example, NG–NG–NG–NG–NG and D–D–D–P–P–P. Here the gradient would be formed by the different position at which D changes to P in packed D/P microfibrils. A high stiffness of 1400 MPa is calculated for the distal end of this assembly decreasing to 140 at the proximal end. Note the 10-fold decrease. Neither of these outcomes specifically matches the actual stiffness of the distal and proximal portions (500 and 50 MPa, respectively). However, the 10-fold change in model B is suggestive. If one were to correct both models using the apparent volume actually occupied by preCOLs as estimated from TEMs of thread sections (*25*), the adjusted stiffness would be 160 and 3 MPa for model A, and 450 and 45 MPa for model B. The striking similarity between the adjusted stiffness of model B and the measured stiffness is tantalizing but does not necessarily strengthen the case in favor of model B given the many assumptions made. Model B does, however, get added support from AFM imaging. Topographical maps based on scanning AFM reveal a lateral uniformity consistent with smectic arrays; more to the point,

preCOL-Ds, which are detectable by their multiple bends, appear to follow one another in axial sequence with a C_2 point group symmetry (Figure 4B) (*18*). This would seem to rule out model A with alternating preCOL-NG. Plausible modeling of the design of natural materials must be tempered by the sobering fourth commandment of biochemistry articulated by Kornberg, "Just because we can explain something does not mean we should believe it" (*26*).

Little has been said so far of the histidine-rich or HIS domains at the N- and C-termini of the preCOLs. These sequences are of two basic types: (1) those with histidine–alanine repeats [HA] and (2) those with histidine–glycine repeats, for example, [HGG]. The former predominate at the N-terminus of preCOL-D and -P, whereas the latter are more abundant at the C-terminus. Curiously, this pattern is reversed in preCOL-NG (*27*). We propose that the HIS domains correspond to the interlocking adaptor regions of LEGO blocks; that is, they mediate axial interactions between preCOLs. Histidines are well equipped to do this given their metal-binding properties. Histidine clusters such as His_6 are widely engineered into proteins to bind proteins to immobilized metal-affinity columns (*28*), as templates for controlled nanocrystal growth (*29*), in ink-jet lithography to metal surfaces (*30*), and as ligands in metal-mediated copolymers (*31*). The location of the HIS domains at the ends of each unit is ideally suited to enable them to function as the couplings or links between units. Whether this is their role in preCOLs has yet to be directly demonstrated. Zn and Cu are present in byssus at concentrations of at least 0.2 wt % (*32–33*). Chelation of metals from byssal threads with EDTA significantly decreases stiffness by 45%; decreasing the pH of the medium from 8.0 to 6.0 lowers the stiffness by nearly 70% (*32*).

Histidine-mediated preCOL couplings are appealing for yet another important reason, that is, speed of formation. Each byssal thread is rapidly made (~5 min), which is necessary because new threads are immediately recruited into tension. Such speed in production is possible in part because holocrine cells in the mussel foot contain secretory granules with prefabricated, stockpiled, and graded preCOL assemblages that are ready to go (*17*,*27*). The assemblages are liquid crystalline (LC) in the sense that they have order and malleability. The granular contents are released into the ventral groove of the foot where they are molded into the shape of a thread by a process resembling reaction-injection molding (*11*) prior to release.

Liquid crystalline polymers typically do not possess adequate cohesive strength without some mechanism for "locking" or "freezing" the structure (*34*, *35*). In spider dragline silk, for example, locking is triggered by strain during fiber drawing, which reportedly helps align the poly-(alanine) β-sheets into nanocrystals (*36*, *37*). The locking mechanisms of byssal threads are still a matter of debate. The traditional model is based on the formation of quinone-derived covalent cross-links between proteins (*38*). Indeed, all necessary ingredients for this mechanism are present in the byssus: 3,4-dihydroxyphenylalanine-containing proteins, catechol oxidase, and dissolved O_2 (*7*, *38*). After several in situ studies, however, it has been conceded that although quinone-derived cross-links are detectable, particularly in the plaque, their concentration is too low and rate of formation too slow to account for the cohesive strength that is immediately evident upon release (*39–41*).

At this time, an initial pH-triggered locking mechanism that is based on transition metals liganded by multiple histidine-rich sequences provides the only explanation consistent with all the experimental data. The pH trigger would presumably be provided by the change in pH from intra-granular (pH 5) to seawater (pH 8). Thread stiffness is significantly decreased by treatment with EDTA or at pH below 7 (*32*). It is possible that the covalent, quinone-derived cross-links make an increasing contribution to cohesiveness with age, but newly formed threads appear to be recruited into tension without them.

Gradients in Polychaete Jaws

The only hard structures in marine polychaetes are the jaws and the bristles (setae). The jaws are well-developed in worms such as *Glycera* and *Nereis*, which use them for grasping, injecting venom into, and dismantling prey. Except for a basal core of pulp cells, the jaws are acellular structures, attached to the cuticle and ligaments at their base. In common with mussel byssal threads, the jaws contain proteins with histidine-rich domains and transition metals, Cu and Zn, and exhibit distinct mechanical gradients.

Although the jaws of *Glycera* and *Nereis* both contain gradients, we shall limit our discussion to the latter because, given their larger size, they lend themselves more readily to gradient analyses. The mechanical properties of jaws have been examined by a technique known as nanoindentation. An excellent and detailed description of this method is available (*42*). In brief, an inverted pyramidal tip mounted onto a stylus-like indenter is pushed into the surface of a material at a selected rate and force. Indentation stiffness (*E*) is determined from the linear part of the load-displacement curve during unloading, whereas hardness (*H*) is calculated from the applied force and imprint area. In the worm jaws, nanoindentation analyses suggest the existence of a mechanical gradient from the tip to the base. Results summarized for a *Nereis* jaw in Figure 6 illustrate that the highest *E* and *H* occur at or near the tip, which is consistent with the penetrating function of this structure (*43*,*44*). The difference in measured indentation stiffness between the tip and the base of dry *Nereis* jaws is about 3-fold. *Glycera* jaw tips are stiffer than those of *Nereis* by a factor of 1.5 and are twice as hard, which is not surprising given their function as hypodermic needles for injecting venom. In *Glycera* jaw, the indentation modulus decreases from tip to base by a factor of 2. There is also another gradient in both worm jaws, which runs longitudinally from the surface to the core. Similar unidirectional gradients engineered into glass–ceramic composites were shown to be superior at suppressing Hertzian-type cracks (*45*). Given that nanoin-dentation studies on polychaete jaws to date have dealt entirely with air-dried samples, the difference between tip–base and surface–core gradients could be greatly enhanced in hydrated analyses especially if tip and base or surface and core hydrate differentially. The effect of hydration on mechanical properties is being actively pursued.

In polychaete jaws, there are two molecular gradients that correlate well with the above-described stiffness and hardness gradients: one is reflected by the distribution of metal ions and the other by variations in the composition of the jaw protein. The biochemical dissection of jaw proteins has not progressed as far as that of byssal threads, but because of the highly biased composition of jaws, the gradient protein distribution is rather apparent from amino acid analyses. *Nereis* jaw protein exhibits glycine and histidine levels of 30 and 20 mol %, respectively, whereas in *Glycera*, the glycine and histidine levels can exceed 60 and 30 mol %, respectively. Because of its larger size, a *Nereis* jaw is more conducive to analysis by section hydrolysis. Figure 7 shows the variation in histidine content as a function of location in one jaw of *Nereis*. Histidine levels are highest at the jaw tip where they reach 22 mol % (*46*) and drop to about 5% at the base. There is a second histidine gradient exhibiting a slight but significant decrease from the toothed inner side to the smoother outer side.

The differential distribution of metals in polychaete jaws was first studied in 1980 (*47*, *48*), at which time it was shown using electron microprobe analysis that *Glycera* jaw has copper at 5–13% dry weight (and traces of Zn); *Nereis* jaw contains up to 3% Zn in dry weight. The metal concentrations were shown to be highest at the jaw tips, decreasing gradually to undetectable levels at the bases. These results were confirmed by synchrotron X-ray fluorescence imaging (Figure 7B shows the Zn distribution in a *Nereis* jaw) (*46*).

Given the similar metal distribution and mechanical gradients in *Nereis* and *Glycera* jaws, a paradoxical but intriguing difference in the chemistry of the metals in the two species has come to light. In *Glycera*, more than half of the copper is associated with a mineral, atacamite (OH_3Cu_2Cl), whereas some of the copper and the small amount of zinc present seem to be bound in macromolecular–metal ion complexes. In *Nereis* jaws, in contrast, despite the 3% w/w levels of zinc, there is no evidence to support a mineral form. Examination of *Nereis* jaws by synchrotron X-ray absorption spectroscopy (XANES and EXAFS) provides the strongest evidence against the presence of a Zn-based mineral. Comparison of the experimental XANES and EXAFS data with those of various Zn salts and calculated spectra of known Zn proteins showed that the best match could be obtained when considering a chemical environment similar to that in the hexamer of Zn-insulin (*46*, *50*) in which the ligands for each Zn^{2+} ion are three histidine residues and a chlorine atom (Figure 8). These results suggest that the metal ions (zinc or copper) might be serving as cross-linkers of histidyl and other ligating functionalities. Thus, as more metal and histidine are available, the cross-linking becomes denser and the structure stiffer. Whether this naïve prediction is played out in these materials following analysis by increasingly sophisticated methods remains to be seen.

Significance of Metals and Histidine

The association of histidine with metal binding is a hallmark of enzyme active site chemistry. Carbonic anhydrase, superoxide dismutase, and tyrosinase have multiple histidine ligands to Cu, Zn, or both as do other proteins such as hemocyanin, insulin, and caeruloplasmin (*51*). Histidine–metal interactions in scaffolding proteins are not as well-known. It is pertinent and intriguing to ask why mussels and worms might prefer histidine–metal motifs to covalent cross-links to stabilize structural proteins. Of course, this can only be speculated upon at this time, but there are some important possibilities: (1) given the physiologically poised pK_a of histidine, histidine–metal interactions can be controllably and instantaneously formed, for example, pH-triggered; (2) they are robust (bond energies up to ~150 kcal/mol, *52*); (3) they are reversible in model peptides through hundreds of pull-to-break cycles as studied by AFM (*53*). The combination of robustness and reversibility is particularly attractive because these features are thought to be important determinants of toughness and self-healing in biomolecular materials (*54*). An engineered β hairpin turn and coiled coil were both found to be stabilized by up to 3 kcal/mol with appropriately engineered histidine–metal–histidine bridges (*55*, *56*). Also, there is a growing database for secondary and tertiary protein structure stabilization with histidine–metal bonds (*57*). A pH-triggered bond formation is expected at physiological pH given that metal binding is usually strongest with the unprotonated δ-1 N of the imidazolate (*58*). A pK_a of 6.5 is viewed as a reasonable estimate for a solvent-accessible isolated histidyl imidazole group (*59*). This, however, can show considerable variation that is dependent on the local microenvironments. His-92 of plastocyanin, for example, which is ligated to a Cu(I) ion, has a pK_a of 5 (*60*). The best-known functional example of histidine–metal binding triggered at least in part by pH is insulin, which gravitates between a stable but inactive Zn-containing hexamer and the active “apo” monomer (*61*).

Ostensibly, jaw proteins with scores of potential metal binding sites should possess very stable mature secondary and tertiary structures. Whether this stability translates to stiffness and hardness has not been demonstrated. Nonetheless, it is tempting to speculate that the metal ion and mineral components make some contribution to the mechanical properties of the jaws, which consist predominantly of organic polymers such as proteins. In epoxy resins, for example, the addition of metals and coordination functionalities improves fracture toughness, thermal stability, and water absorption (*62*). Using an Ashby plot (*3*), jaw hardness and stiffness is compared with various organic synthetic polymers (Figure 9). Note that with only a few percent Zn ions, *Nereis* jaw protein, which lacks mineral, achieves hardness and stiffness that is 2–3 times higher than the best competition. Similarly, *Glycera* jaw exhibits an order of

magnitude higher performance in mechanical properties by inclusion of a mere 10% atacamite by weight. Both jaws rank well in hardness with dentin, which contains over 70% mineral by weight (Figure 9). The plot suggests that engineering extensive metal binding functionalities and metal ions into a polymer scaffold may offer an alternative way to tune the hardness, stiffness, or both of a material thus avoiding a heavy reliance on mineralization and reducing the weight as well.

Concluding Remarks

We have presented two structures in which mechanical gradients appear to be closely correlated with molecular gradients. There have been other such studies, for example, the dentinoenamel junction in tooth (*63*), and it would not surprise us if biology used gradients de rigueur in the construction of scaffolds, but there have been few studies of this at the molecular level. Suresh (*1*) attributed the appeal of gradients in manufactured structures to the following advantages: gradients smooth stress distribution, eliminate stress singularities, reduce stress concentration, improve bonding strength, and increase fracture toughness. The evolution of biological structures cannot be “blind” to such advantages, and much can be learned from the adaptive “designs” of natural scaffolding materials. Analytical tools devised for disciplines as diverse as materials science, biophysics, and physical chemistry are proving increasingly useful for characterization of biological structures including byssal threads and jaws but still have limitations given the history of their development for very different sorts of problems and materials.

The major mechanical challenge at present involves enabling reliable mechanical characterization under hydrated physiological conditions and real time. This is being increasingly addressed in AFM and nanoindentation, but there is much room for improvement. In byssal threads, for example, it would be desirable to know more about the lateral and axial interactions of preCOLs in the nanometer range, as well as the subtleties of gradient properties over hundreds of micrometers. AFM may be approaching the requisite level of refinement for the in situ measurement of the stiffness of specific protein domains (*64*), whereas the expanded resolution of mechanical resonance (*65*) should be useful for the characterization of mechanical gradients in long biofibers.

Challenges in the microchemical analysis of biological structures are considerable. Although elemental analysis has seen a gradual improvement in detection limits and spatial resolution, the information though useful is still largely empirical. IR/Raman microprobes (*66*) and synchrotron X-ray absorption are offering glimpses of higher-order biological structure and organization that will become increasingly revealing as the database expands.

Acknowledgements

We thank Les Wilson and Eleni Kousvelari for their encouragement and Frank Zok for introducing us to Ashby plots.

References

1. Suresh S. Graded materials for resistance to contact deformation and damage. Science 2001;292:2447–2451. [PubMed: 11431558]
2. Vogel, S. Comparative Biomechanics. Princeton University Press; Princeton, NJ: 2003. p. 175-200.
3. Ashby MF. Materials in mechanical design. Mater Res Soc Bull 1993;18:43–53.
4. Gosline JM, Guerette PA, Ortlepp CS, Savage KN. The mechanical design of spider silks: from fibroin sequence to mechanical function. J Exp Biol 1999;202:3292–3305.
5. Vincent, JFV. Structural Biomaterials. Princeton University Press; Princeton, NJ: 1990.
6. Kinloch, AJ. Adhesion and Adhesives: Science and Technology. Chapman and Hall; London: 1987. p. 204

7. Waite JH. Adhesion a la moule. Integr Comp Biol 2002;42:1172–1180.
8. McWhirter MJ, Bremer PJ, Lamont IL, McQuillan AJ. Siderophore mediated covalent binding to metal (oxide) surfaces during biofilm initiation by *Pseudomonas aeruginosa* bacteria. Langmuir 2003;19:3575–3577.
9. Gosline JM, Lillie M, Carrington E, Guerette PA, Ortlepp CS, Savage KN. Elatomeric proteins: biological roles and mechanical properties. Philos Trans R Soc London B 2002;357:121–132. [PubMed: 11911769]
10. Vollrath F, Knight DP. Liquid crystalline spinning of spider silk. Nature 2001;410:541–548. [PubMed: 11279484]
11. Waite JH. Anatomy of a natural manufacturing process. Results Probl Cell Differ 1992;19:27–54. [PubMed: 1289996]
12. Waite JH, Qin X, Coyne KJ. The peculiar collagens of mussel byssus. Matrix Biol 1 1998;7:93–108.
13. Komatsu K. Fiber formation and chemistry of silk protein. Hikaku Kagaku 1982;28:1–20.
14. Lucas F, Shaw JTB, Smith SG. The chemical composition of some silk fibroins and its bearing on their physical properties. J Text Inst T 1955;46:440–452.
15. Kilchherr E, Hoffmann H, Steigemann W, Engel J. Structural model of the collagen-like region of C1q comprising the kink region and the fiberlike packing of six triple helices. J Mol Biol 1985;186:403–415. [PubMed: 3878889]
16. Qin X, Coyne KJ, Waite JH. Tough tendons: mussel byssus has collagen with silk-like domains. J Biol Chem 1997;272:32623–32627. [PubMed: 9405478]
17. Vitellaro-Zucarrello L. The collagen gland of *Mytilus galloprovincialis*: an ultrastructural and cytochemical study on secretory granules. J Ultrastruct Res 1980;73:135–147. [PubMed: 7194382]
18. Hassenkam T, Gutsmann T, Hansma P, Sagert J, Waite JH. Giant bent-core mesogens in the thread forming process of marine mussels. Biomacromolecules. in press
19. Qin X, Waite JH. Exotic collagen gradients in byssal threads of *Mytilus edulis*. J Exp Biol 1995;198:633–644. [PubMed: 7714453]
20. Tamarin A, Lewis P, Askey J. The structure and formation of the byssal attachment-forming region in *Mytilus californianus*. J Morphol 1976;149:199–221. [PubMed: 933173]
21. Sun CJ, Lucas JM, Waite JH. Collagen binding matrix proteins from elastomeric extra-organismic byssal threads. Biomacromolecules 2002;3:1240–1248. [PubMed: 12425661]
22. Parry DAD, Steinert PM. Intermediate filaments: molecular architecture, assembly, dynamics, and polymorphism. Q J Biophys 1999;32:99–187.
23. Wainwright, SA.; Biggs, WD.; Currey, JD.; Gosline, JM. Mechanical Design in Organisms. Princeton University Press; Princeton, NJ: 1982. p. 145-148.
24. Waite JH, Vaccaro E, Sun CJ, Lucas JM. Elastomeric gradients: A hedge against stress concentration in marine holdfasts. Philos Trans R Soc London B 2002;357:143–153. [PubMed: 11911771]
25. Bairati A, Vitellaro-Zuccarello L. The ultrastructure of the byssal apparatus of *Mytilus galloprovincialis*. Cell Tissue Res 1976;166:219–234. [PubMed: 1248045]
26. Kornberg A. Ten commandments of enzymology, amended. Trends Biochem Sci 2003;28:515–517. [PubMed: 14559177]
27. Qin X, Waite JH. A potential mediator of collagenous block copolymer gradients in mussel byssal threads. Proc Natl Acad Sci USA 1998;95:10517–10522. [PubMed: 9724735]
28. Arnold, FH. Metal Affinity Protein Separations. Academic Press; San Diego, CA: 1992.
29. Djalali R, Chen Y, Matsui H. Au nanocrystal growth on nanotubes controlled by conformations and charges of sequenced peptide templates. J Am Chem Soc 2003;125:5873–5879. [PubMed: 12733928]
30. Agarwal G, Naik RR, Stone MO. Immobilization of histidine-tagged proteins on nickel by electrochemical dip pen nanolithography. J Am Chem Soc 2003;125:7408–7412. [PubMed: 12797815]
31. Wang C, Stewart RJ, Kopecek J. Hybrid hydrogels assembled from synthetic polymers and coiled coil domains. Nature 1999;397:417–420. [PubMed: 9989405]
32. Vaccaro E, Waite JH. Yield and post-yield behavior of mussel byssal threads: A self-healing biomolecular material. Biomacromolecules 2001;2:906–911. [PubMed: 11710048]

33. Coombs TJ, Keller PJ. *Mytilus* byssal threads as an environmental marker. Aquat Toxicol 1981;1:291–300.
34. Sapich B, Stumpe J, Kricheldorf HR, Fritz A, Schonhals A. Synthesis, dielectric, photochemical study of liquid crystalline main chain polyester imides containing cinnamoyl moieties. Macromolecules 2001;34:5694–5701.
35. Hanabusa K, Suzuki T, Koyama T, Shirai H. Effect of metal complexation on the behavior of a liquid crystalline polymer. J Macromol Sci A 1990;27:1379–1387.
36. Kerkam K, Viney C, Kaplan D, Lombardi S. Liquid crystallinity of natural silk secretions. Nature 1991;349:596–598.
37. Viney, C. Silk fibers: Origins, nature and consequences of structure. In: Elices, M., editor. Structural Biological Materials. Pergamon; Amsterdam: 2000.
38. Burzio LA, Waite JH. Cross-linking in adhesive quinoproteins: studies with model decapeptides. Biochemistry 2000;39:11147–11153. [PubMed: 10998254]
39. Klug CA, Burzio LA, Waite JH, Schaefer J. In situ analysis of peptidyldopa in mussel byssus using rotational double echo resonance NMR. Arch Biochem Biophys 1996;333:221–224. [PubMed: 8806774]
40. Holl SM, Hansen D, Waite JH, Schaefer J. Solid-state NMR analysis of cross-linking in mussel protein glue. Arch Biochem Biophys 1993;302:255–258. [PubMed: 8470902]
41. McDowell LM, Burzio LA, Waite JH, Schaefer J. REDOR detection of cross-links formed in mussel byssus under high flow stress. J Biol Chem 1999;274:20293–20295. [PubMed: 10400649]
42. Oliver WC, Pharr GM. An improved technique for determining hardness and elastic modulus using load and displacement sensing indentation experiments. J Mater Res 1992;7:1564–1583.
43. Lichtenegger HC, Schöberl T, Bartl MH, Waite JH, Stucky GD. High abrasion resistance with sparse mineralization: Copper biomineral in worm jaws. Science 2002;298:389–392. [PubMed: 12376695]
44. Lichtenegger HC, Schöberl T, Bartl MH, Waite JH, Stucky GD. Response to comment on “High abrasion resistance with sparse mineralization: Copper biomineral in worm jaws”. Science 2003;301:1049b. [PubMed: 12933994]
45. Pender DC, Padture NP, Giannakopoulos AE, Suresh S. Gradients in elastic modulus for improved contact damage resistance. Acta Mater 2001;49:3255–3262.
46. Lichtenegger HC, Schöberl T, Ruokolainen J, Cross JO, Heald SM, Birkedal H, Waite JH, Stucky GD. Zinc and mechanical prowess in the jaws of *Nereis*, a marine worm. Proc Natl Acad Sci USA 2003;100:9144–9149. [PubMed: 12886017]
47. Bryan GW, Gibbs PE. Zinc – the major inorganic component of Nereid jaws. J Mar Biol Assoc U K 1979;59:969–973.
48. Bryan GW, Gibbs PE. Metals in nereid polychaetes: the contribution of metals in the jaws to the total body burden. J Mar Biol Assoc U K 1980;60:641–654.
49. Gibbs PE, Bryan GW. Copper – the major inorganic component of glycerid polychaete jaws. J Mar Biol Assoc U K 1980;60:205–214.
50. Smith GD, Swenson DC, Dodson EJ, Dodson GG, Reynolds CD. Structural stability in the zinc insulin hexamer. Proc Natl Acad Sci USA 1984;81:7093–7097. [PubMed: 6390430]
51. Holm RH, Kennepohl P, Solomon EI. Structural and functional aspects of metal sites in biology. Chem Rev 1996;96:2239–2214. [PubMed: 11848828]
52. Deng H, Kebarle P. Bond energies of copper ion ligand L complexes CuL_2^+ determined in the gas phase by ionligand exchange equilibria measurements. J Am Chem Soc 1998;120:2925–2931.
53. Schmitt L, Ludwig M, Gaub HE, Tampe R. A metal chelating microscopy tip as a new tool box for single molecule experiments by atomic force microscopy. Biophys J 2000;78:3275–3285. [PubMed: 10828003]
54. Thompson JB, Kindt JH, Drake B, Hansma HG, Morse DE, Hansma PK. Bone indentation recovery time correlates with bond reforming time. Nature 2002;414:773–776. [PubMed: 11742405]
55. Krantz BA, Sosnick TR. Engineered metal binding sites map the heterogeneous folding landscape of a coiled coil. Nat Struct Biol 2001;8:1042–1047. [PubMed: 11694889]
56. Platt G, Chung CW, Searle MS. Design of histidine Zn+2 binding sites within a beta hairpin peptide: enhancement of beta sheet stability through metal complexation. Chem Commun 2001:1162–1163.

57. Bell AJ, Xin H, Taudte S, Shi ZS, Kallenbach NR. Metal dependent stabilization of an active HMG protein. Protein Eng 2002;15:817–825. [PubMed: 12468716]
58. Smith MC, Furman TC, Pidgeon C. Immobilized imidodiacetic acid metal peptide complexes. Identification of chelating peptide purification handles for recombinant proteins. Inorg Chem 1987;26:1965–1969.
59. Kyte, J. Structure in Protein Chemistry. Garland Publ Inc: New York; 1995. p. 424-425.
60. Hass MAS, Tuesen MH, Christensen HEM, Led JJ. Characterization of ms-ms dynamics of proteins using a combined analysis of 15N NMR relaxation and chemical shift: conformational exchange in plastocyanin induced by histidine protonations. J Am Chem Soc 2004;126:753–765. [PubMed: 14733549]
61. Søndergaard LG, Stoltenberg M, Flyvbjerg A, Brock B, Schmitz O, Danscher G, Rungby J. Zinc ions in the beta cells of obese insulin resistant and type 2 diabetic rats traced by autometallography. APMIS 2003;111:1147–1154. [PubMed: 14678025]
62. Hamerton I, Howlin BJ, Jepson P. Metals and metal coordination compounds as modifiers for epoxy resins. Coord Chem Rev 2002;224:67–82.
63. Marshall GW, Balooch M, Gallaghar RR, Gansky SA, Marshall SJ. Mechanical properties of the dentinoenamel junction: AFM studies of nanohardness, elastic modulus and fracture. J Biomed Mater Res 2001;54:87–95. [PubMed: 11077406]
64. Li H, Oberhauser AF, Redick SD, Carrion-Vazquez M, Erickson HP, Fernandez JM. Multiple conformations of PEVK proteins detected by single molecule techniques. Proc Natl Acad Sci USA 2001;98:10682–10686. [PubMed: 11526214]
65. Dikin DA, Chen X, Ding W, Wagner G, Ruoff RS. Resonance vibration of amorphous SiO2 nanowires driven by mechanical or electrical field excitation. J Appl Phys 2003;93:226–230.
66. Dong J, Atwood CS, Anderson VE, Siedlak SL, Smith MA, Perry G, Carey PR. Metal binding and oxidation of amyloid-β within isolated senile plaque cores: Raman microscopic evidence. Biochemistry 2003;42:2768–2773. [PubMed: 12627941]

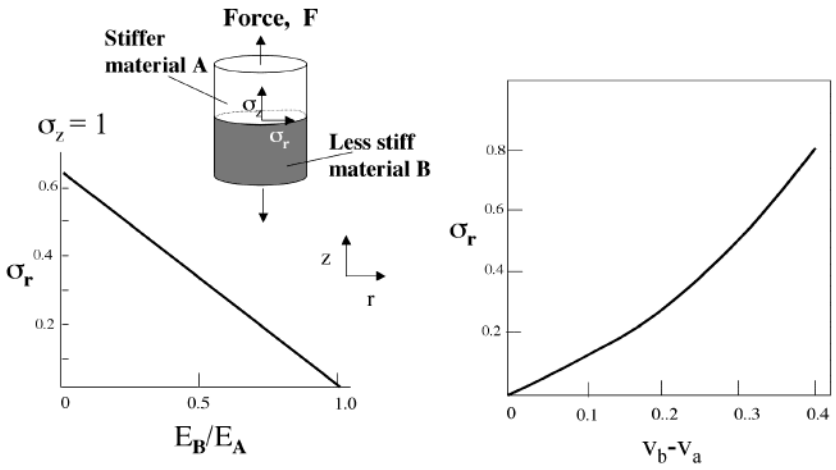

Figure 1.

Radial stress, σ_r, in a butt joint made of two materials having different stiffness (E_i). Graph A shows how σ_r increases as the stiffness of B decreases relative to A, fixing the Poisson ratio of both at 0.4. Graph B shows how σ_r increases as the difference between Poisson ratios of ν_A and ν_B increases at a fixed stiffness ratio of 1. A nominal axial stress σ_z =1 is assumed.

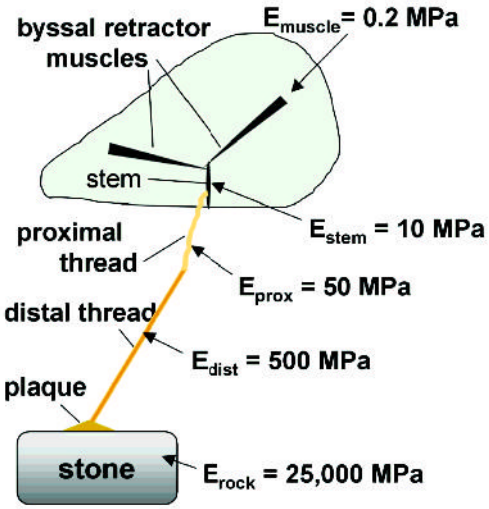

Figure 2.
Schematic mussel on the half-shell with one byssal thread showing the incremental steps in stiffness, E_i, from the retractor muscles to the rock. Note the 10-fold decrease in stiffness between the distal and proximal portions of the thread (adapted from ref 26).

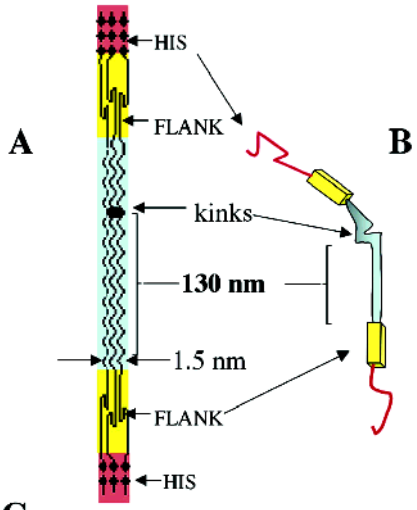

C

PreCol	*Flank prototype*	*Sequence*	*Stiffness MPa*
D	**Silk fibroin**	**$\{[A_{10}](GGX)_3\}_7$**	**10,000**
P	**Elastin**	**$(XGXPG)_{10}$**	**2**
NG	**Poly-Glycine**	**$(GGGX)_{70}$**	**150**
	Core prototype		
	Collagen	**$(Gly\text{-}X\text{-}Y)_{170}$**	**1,500**

Figure 3.

Proposed structure of the preCOLs making up the bulk of each mussel byssal thread. The block domain structure in 2D of a trimer is shown in panel A; the bent-core analogue of a trimer is shown in panel B; amino to carboxy terminal orientation is top-to-bottom. Summary of sequence features of each flank type and estimated stiffness constants (panel C) are as described in text. X represents any amino acid except glycine and alanine. Stiffness represents the initial modulus determined for fully hydrated biopolymers including the alanine-rich fibroin of *Anaphe* silk (*14*).

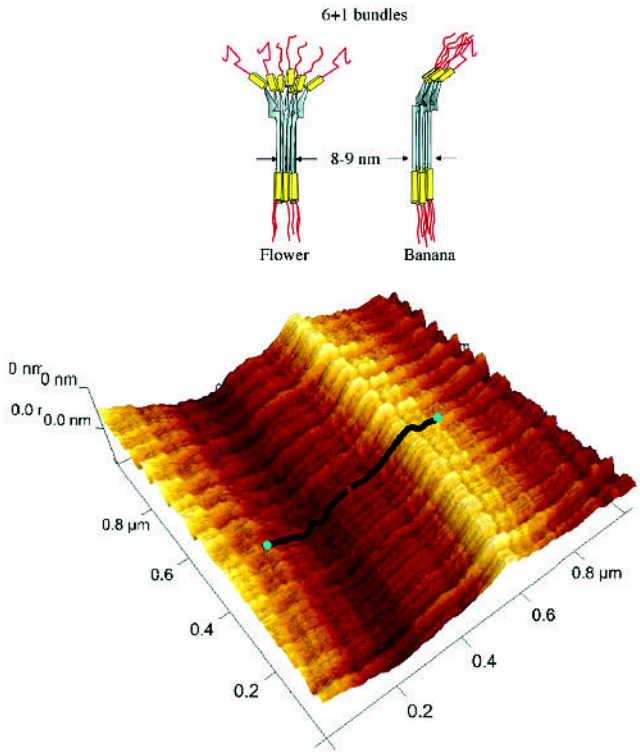

Figure 4.
Model of the hexagonal (6 + 1) bundles of bent-core trimers in the flower and banana configurations (top) and AFM image of a smectic array of preCOL-D bundles in the proximal portion of the thread stretched by at least 100% (bottom). A pair of overlaid model molecules related by a C_2 point symmetry is shown in black with the N-termini in blue (reprocessed data from ref 18).

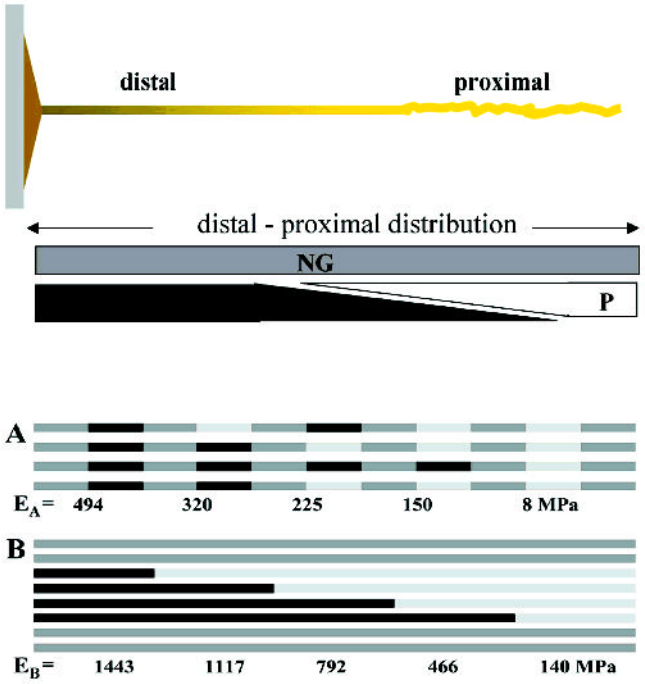

Figure 5.

Distribution of different preCOLs along a byssal thread. Gradients of preCOL-D (D) and preCOL-P (P) in the thread (top) indicate that preCOL-D predominates in the distal portion, whereas preCOL-P predominates in the proximal portion. PreCOL-NG is uniformly present all along the thread. Possible relationship between preCols in the transitional region according to two assembly models A and B (bottom) is represent by PreCol-D (black), preCol-NG (gray), and preCol-P (white). The elastic modulus calculated according to the Voigt equation appears below each increment.

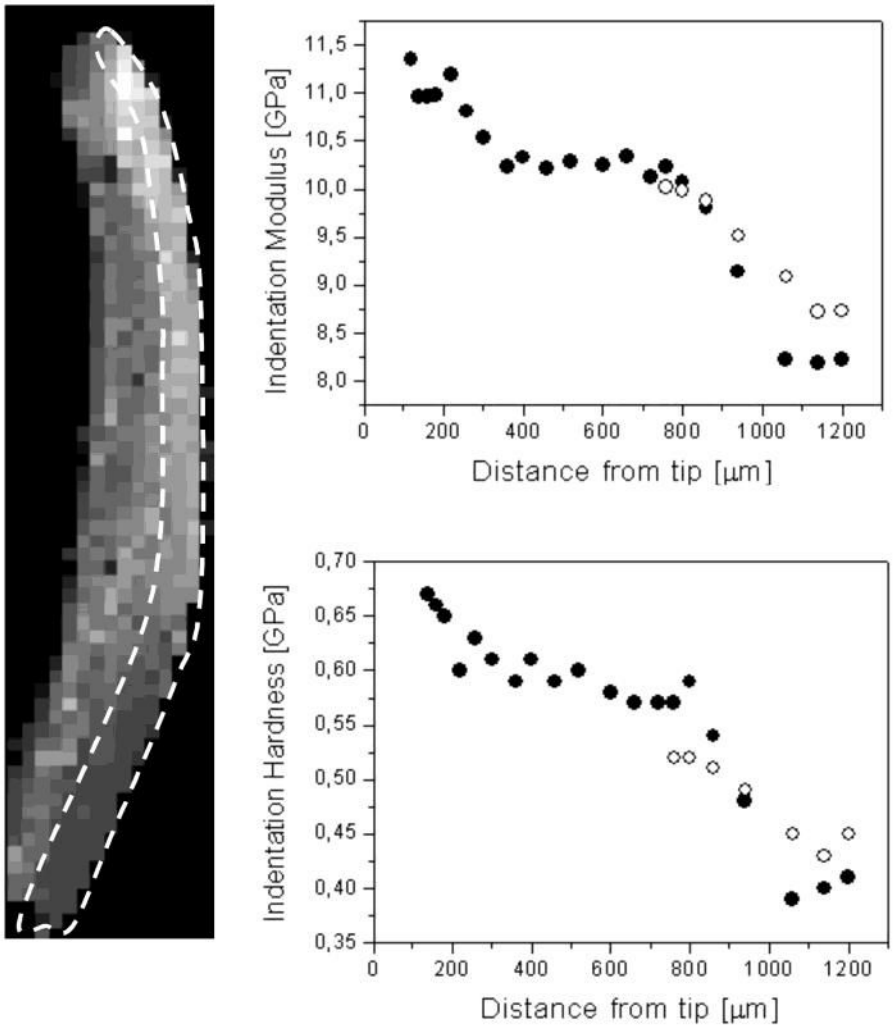

Figure 6.

Indentation stiffness and hardness measurements in *Nereis* jaw. The left panel shows a pixilated longitudinal section of the jaw tip; each pixel corresponds to an actual indentation measurement, the brightness being indicative of the local stiffness value. The circumscribed area highlights the region examined for gradients. The right panel presents plots showing the variation of indentation stiffness and hardness along the outer jaw curvature measured from the tip, which is at the top of the image. Specimen dimensions are 0.3 mm × 1.4 mm; pixel size is 20 μm × 20 μm.

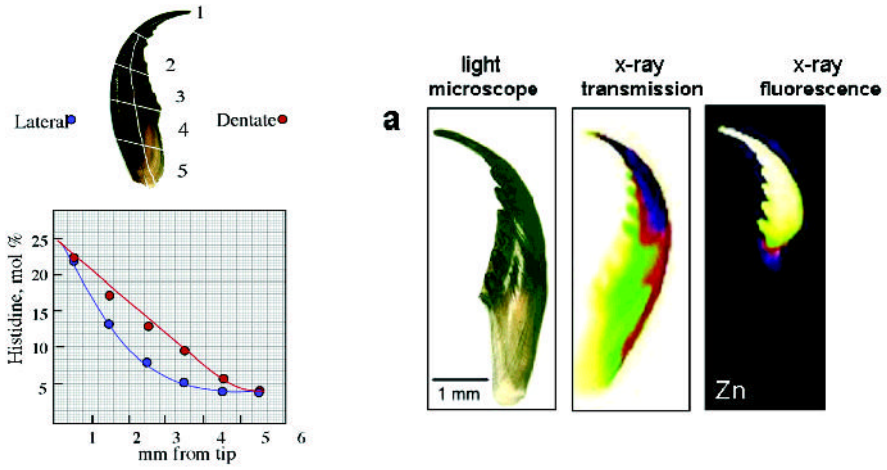

Figure 7.

Gradients in the tip-to-base histidine and zinc distribution of a *Nereis* jaw (from ref 45). The left panel shows a sketch of a *Nereis* jaw sectioned for amino acid analysis (top) and the decrease of histidine content (bottom) from ~22 mol % at the tip to 5 mol % at the base and lateral to serrated side of the *Nereis* jaw. The right panel shows the Zn-fluorescence mapping with synchrotron radiation. Images from left to right display a light microscopic image of intact *Nereis* jaw, an X-ray absorption image (the dark region at the tip denotes greater absorption), and an X-ray fluorescence image (lighter colors indicate greater amount of Zn).

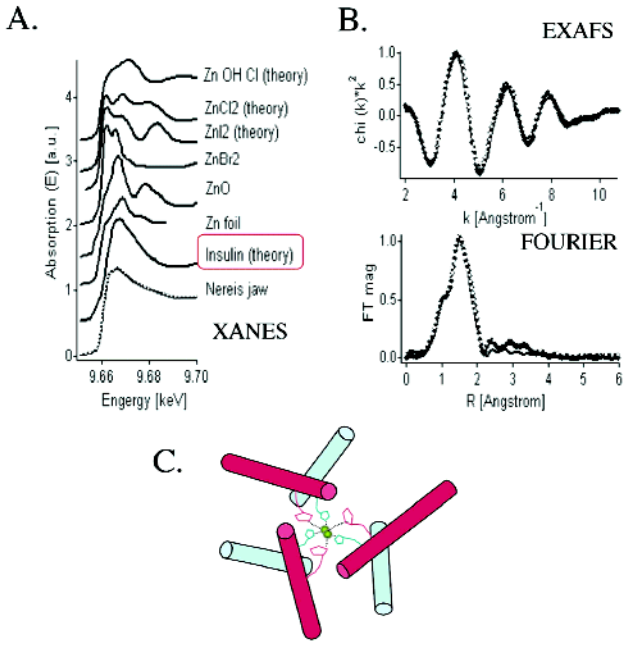

Figure 8.

Synchrotron X-ray absorption spectroscopy of *Nereis* jaw. Panel A shows comparative XANES of *Nereis* jaw, miscellaneous zinc-containing compounds, and Zn-insulin. *Nereis* jaw and Zn-insulin are the best fit. Panel B shows experimental Zn-EXAFS data of *Nereis* jaw (black dots), fitted with calculated curves of Zn-insulin (data shown in *k*-space and *R*-space). Comparison shows that the ligand environment of Zn in Nereis jaws is consistent with the presence of histidine. Panel C shows a simplified model of the Zn-insulin hexamer showing coordination of two zinc ions by six histidine ligands. Cl and water ligands are omitted.

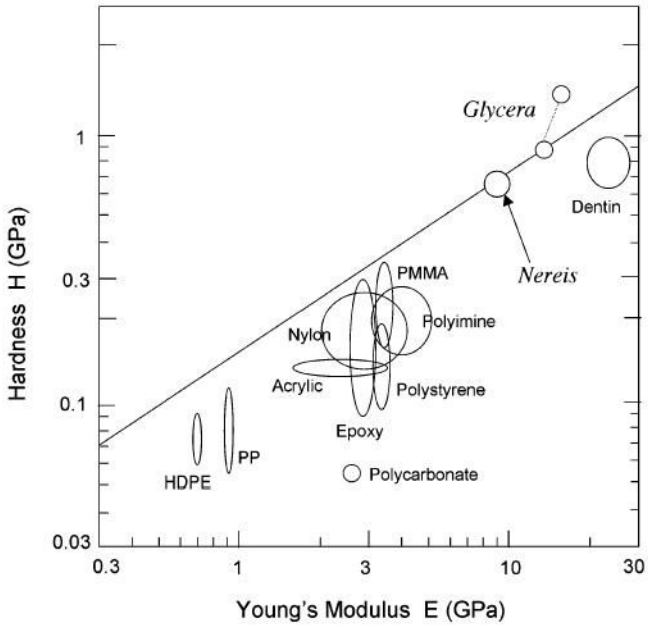

Figure 9.

Ashby plot (*3*) comparing the hardness and stiffness of various organic polymers with those of *Glycera* and *Nereis* jaws, as well as dentin. The two spots for *Glycera* represent properties of the jaw tip (upper) and base (lower); the latter and the *Nereis* spot represent the effect of metal ions only.